Synergetic regulation of CeO$_2$ modification and (W$_2$O$_7$)$^{2-}$ intercalation on NiFe-LDH for high-performance large-current seawater electrooxidation

Mingzhe Li [a,1], Hua-Jie Niu [b,1], Yilong Li [a], Jiawei Liu [a], Xiayuan Yang [a], Yuzhen Lv [a,*], Kepi Chen [a], Wei Zhou [b,*]

[a] *School of Energy, Power and Mechanical Engineering, North China Electric Power University, Beijing 102206, China*
[b] *School of Chemistry, Beijing Advanced Innovation Center for Biomedical Engineering, Beihang University, Beijing 100191, China*

ARTICLE INFO

ABSTRACT

Four-electron process and the interference of Cl$^-$ make sluggish kinetics on oxygen evolution reaction (OER) for seawater electrolysis. Herein, NiFe LDH grown on NiFe-foam with CeO$_2$ modification and (W$_2$O$_7$)$^{2-}$ intercalation was synthesized by one-step hydrothermal method. It only needs 353.8 and 386.7 mV to achieve a large current density of 1000 mA·cm^{-2} in 1 M KOH and alkaline natural seawater, respectively. The catalytic material can stand 100 h with a retention of 98.1% at 1000 mA·cm^{-2} in alkaline natural seawater. Experiments and theoretical calculations confirm that the state-of-the-art OER activity comes from the introduced CeO$_2$ with optimized adsorption energy of intermediates. The improved stability and selectivity in seawater can be ascribed to the preferential adsorption of Ni and Fe with higher valence on OH$^-$ based on hard and soft acid based (HSAB) principle by (W$_2$O$_7$)$^{2-}$ intercalation. This work provides a viable approach to develop efficient catalytic material for large-current seawater electrolysis.

1. Introduction

Hydrogen production by water electrolysis is a potential renewable energy conversion technique to reduce fossil fuel consumption [1]. Highly purified water is required by current electrolysis technology, but in fact 96.5% of the planet's total water retains in the oceans [2]. Therefore, direct seawater electrolysis has higher social and economic benefits due to the preciousness of fresh water resources [3]. It's well known that the oxygen evolution reaction (OER) is one of the key steps in water electrolysis, which has slow kinetic process because of 4-electron transfer and greatly limits the overall efficiency of water splitting [4,5]. Although the theoretical potential for hypochlorite formation is around 490 mV higher than that of OER under the near-neutral or alkaline media (pH>7.5), it can still influence the OER process especially at high current density. [6]. In particular, it cannot be ignored that chloride ions can occupy the active sites of OER causing more sluggish kinetic process, as well as corrode catalytic material via metal chlorination reactions leading to poor stability [7]. Therefore, high-efficiency and robust catalytic materials for OER process with cost advantage are required to ensure large-scale seawater electrolysis [8].

Three main points might be considered for fabricating high-performance electrocatalyst in seawater electrolysis. Firstly, the catalyst might exhibit excellent OER catalytic performance, especially limit the overpotential of OER within ~490 mV even at industrial high current density of 1000 mA·cm^{-2} to avoid hypochlorite formation [9]. Secondly, it also needs to show selective adsorption of hydroxyls (OH$^-$) and anti-interference property of chloride ions in the system full of chloride ions [7]. Thirdly, some impurities such as insoluble substances and microorganisms from natural seawater might cover the catalyst surface, leading to decreased catalytic activity [10]. The third point can be alleviated through simple filtration, so it is important to develop efficient electrocatalysts for seawater oxidation considering the first and the second points.

Typically, Ni-Fe layered double hydroxides (NiFe-LDHs) has been proven to be one of the most active catalysts for fresh water oxidation especially in alkaline environment [11,12]. However, pure LDH catalyst cannot provide suitable overpotential under 490 mV at high current densities in seawater because its high starting potential, intrinsic poor conductivity and weak OH$^-$ selectivity [13–15]. Recently, the introduction of heterointerfaces can improve the OER performance in

---

seawater electrolysis. For example, Dai et al. have developed a heterogeneous $NiFe/NiS_x$ catalyst grown on nickel foam. Especially the sulphate passivation layer derived from NiS_x provides anti-chloride property, improving the OER activity in seawater [16]. The above action can achieve stable catalysis for more than 1000 h under the condition of industrial current density (0.4–1 A·cm^{-2}). Some work indicates that regulating the binding energy of intermediate on catalysts during OER process is beneficial to reduce the starting potential [17,18]. For instance, Ce-based nanomaterials such as CeO_2 can reduce the adsorption free energy by forming strong electron interaction with the actual catalytic active components (FeOOH, NiOOH) in NiFe LDHs [19–21]. In view of the competitive adsorption between Cl^- and OH^- towards active sites in seawater electrolytes, it is necessary to design catalytic materials with OH^- selectivity. Zhang et al. designed a sandwich-type sample of $NiCo(HPO_4)_2$ @Ni_3N/NF, in which the hydrogen phosphate ions achieve the OH^- selectivity in seawater electrolytes by exerting strong Lewis acidity [22]. Because harder acids preferentially bind to harder bases (where OH^- is a harder base than Cl^-) according to the Pearson's HSAB principle [23]. Similarly, Zhou et al. found that the Ni and Fe sites in partially crystallized NiFe LDH have higher valence states than those in fully crystallized NiFe LDH, meaning stronger Lewis acidity and thus improving the OH^- selectivity in seawater electrolytes [18]. Researches show that the Lewis acidity of NiFe LDH can be enhanced by adding alien species with strong Lewis acidity. For example, W(VI) can not only increase the Lewis acidity of NiFe LDH [24], but also induce lattice tensile strain to promote OER. Therefore, we use the strategy of introducing $(W_2O_7)^{2-}$ to enhance the Lewis acidity of NiFe LDH and then to achieve high selectivity towards OH^- instead of Cl^- [24,25].

In this work, we proposed creatively to introduce $(W_2O_7)^{2-}$ intercalation in NiFe LDH to adjust the valence of Ni and Fe elements combined with CeO_2 modifying, which can be used as an efficient and robust industrial catalyst for seawater electrolysis. The designed catalyst only needs 353.8 mV overpotential at 1 M KOH to achieve a current density of 1000 mA·cm^{-2} and a low Tafel slope of 64.4 mV·dec^{-1}. Notably, only 386.7 mV overpotential can achieve a 1000 mA·cm^{-2} current density in alkaline natural seawater, which can operate for 100 h. Experiments and theoretical calculations confirmed the effects of the intercalated $(W_2O_7)^{2-}$ and modified CeO_2 with oxygen vacancies. This work provides a convenient strategy for designing high-efficiency catalysts for high-current alkaline seawater electrolysis.

2. Results and discussion

2.1. Characterizations on morphology, structure, and compositions

The CeO_2 decorated NiFe LDH with $(W_2O_7)^{2-}$ intercalation grown on nickel iron foam (marked as NiFe LDH-CeW@NFF) was fabricated via a facile and scalable one-step hydrothermal method (Fig. 1a). Firstly, the washed NiFe foam (NFF) was placed in a high-pressure reaction kettle containing the mixture of $FeCl_3·6 H_2O$, $Ce(NO_3)_3·6 H_2O$, and $(NH_4)_{10}H_2(W_2O_7)_6·5 H_2O$, which was then placed in an oven at 160 °C for 8 h (detailed synthesis process was provided in Supporting Information). After the hydrothermal reaction process, the NiFe LDHs were grown on NFF substrate. Meanwhile, the CeO_2 particles were decorated on NiFe LDH sheets, while the negatively charged $(W_2O_7)^{2-}$ were intercalated between atomic layers of LDH.
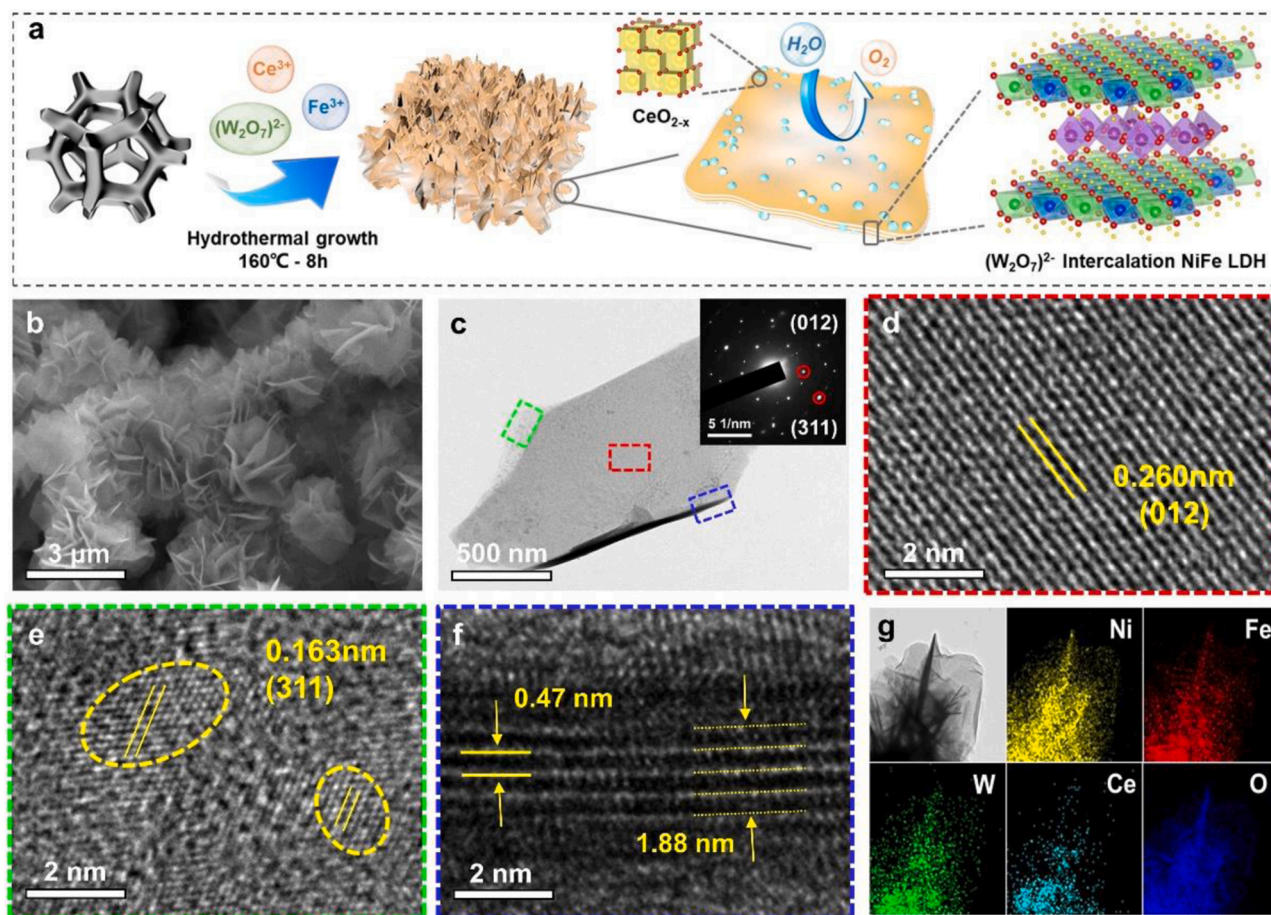

Fig. 1. (a) Schematic illustration for the formation of the NiFe LDH-CeW@NFF. (b) SEM image and (c) TEM images of NiFe LDH-CeW@NFF. The inset is the corresponding SAED pattern. (d-f) HRTEM images corresponding to the marked color frames in (c). (g) TEM image and related EDS mapping of Ni, Fe, W, Ce and O elements for NiFe LDH-CeW@NFF.

The SEM images of NFF with smooth surface was shown in Fig. S1. After the hydrothermal process, some flower-like particles composed of interconnected sheets were grown on NFF (Fig. 1b). By observing the above samples, we found the counterparts of NiFe LDH@NFF, NiFe LDH-W@NFF and NiFe LDH-Ce@NFF have the similar structure like NiFe LDHs-CeW@NFF. On the reticular skeletons of NFF, many microflowers were grown assembled by nanosheets (Fig. S2). TEM image in Fig. 1c showed one typical nanosheet exfoliated from the flower-like structure (Fig. S3). The inset with two sets of spots shows the single-crystal structures of NiFe-LDH (red circles) and CeO_2 (green circles) [26]. We then examined the HRTEM images taken from three regions in Fig. 1c. Fig. 1d corresponding to the red frame shows spacing of 0.26 nm, which can be ascribed to the (012) crystal planes of NiFe LDH [27]. Fig. 1e shows the (311) planes of CeO_2 with spacings of 0.16 nm [28,29]. By observing the single-crystal regions, we can find CeO_2 grains are about 2–4 nm in size grown on the surface of NiFe-LDH. Fig. 1f selected from the section of the sheet, show an obvious interlayered spacing of 0.47 nm. It has been expanded about 0.07 nm compared with the interlayer spacing (0.396 nm) of (006) planes of NiFe LDH [6]. As disclosed by AFM, Fig. S4 shows the thickness of LDH layer is about 1.9 nm. As marked, the HRTEM image in Fig. 1f shows five mono-layers of LDH, close to the thickness of 1.9 nm. The EDS elemental mapping in Fig. 1g verifies the hybrid composition and uniform distribution of Ni, Fe, Ce, W, and O elements in NiFe LDH-CeW@NFF layer. The atomic ratio of Ni: Fe:Ce:W is about 15.5:5.5:2.9:1.7 as disclosed by EDS in Fig. S5.

To further clarify the composition and surficial environment of the catalyst, X-ray diffraction (XRD), Fourier transform infrared spectroscopy (FT-IR) and X-photoelectron spectroscopy (XPS) were carried out and their results are shown in Fig. 2. For the XRD pattern of NiFe LDH-CeW@NFF (Fig. 2a), the peaks marked by triangle at 28.5°, 33.1°, 47.5° and 56.3° correspond to the CeO_2 phase (PDF # 43–1002), while the diffraction peaks at 11.3°, 22.7°, 34.4°, 38.8°, 46.0°, 60.0° and 61.3° can be assigned to the (003), (006), (012), (015), (018), (110) and (113) planes of NiFe LDH (PDF # 38–0715), respectively. [30,31]. Partial XRD

pattern was magnified and shown in Fig. 2b. We can find that the diffraction peaks corresponding to (003) and (006) planes both shift negatively by 0.225° and 0.332°, respectively, which reflects the expansion of interlayer spacing of LDH along *c*-axis caused by intercalated $(W_2O_7)^{2-}$ anions. The inset vividly shows the process of enlarged interlayer spacing. The FT-IR result in Fig. 2c shows the O-H bending vibration mode corresponding to the strong peak at 1623 cm^{-1} [32], which might come from adsorbed water molecules. The peak at 1354 cm^{-1} corresponds to Cl^-, which might from the residue from the synthetic process. Notably, the inset shows the enlarged part of the marked region, revealing the vibration of W-O cluster skeleton at 923 cm^{-1} [24]. It confirms the successful insertion of $(W_2O_7)^{2-}$ anions. The peaks at 488 and 513 cm^{-1} correspond to the bending vibration modes of Ni-O and Fe-O, respectively [33]. The peak at 643 cm^{-1} corresponds to the lattice vibration mode of M-O-H [34]. The other peaks at 460 cm^{-1} can verify the existence of CeO_2, and the extremely weak signal at 1118 cm^{-1} might come from the overtone band of trace Ce-OH because of adsorbed water molecules on its surface [35]. The above analysis combined with TEM and XRD results confirm the existence of NiFe-LDH, CeO_2, and $(W_2O_7)^{2-}$.

For comparison, we chose NiFe-LDH@NFF, NiFe-LDH with CeO_2 decoration (NiFe LDH-Ce@NFF), NiFe-LDH with $(W_2O_7)^{2-}$ insertion (NiFe LDH-W@NFF) as counterparts to disclose the effect of introduced CeO_2 and $(W_2O_7)^{2-}$. The XPS survey spectrum (Fig. S6) reveals the coexistence of Ni, Fe, Ce and W elements in NiFe LDH-CeW@NFF in addition to O and C species adsorbed on the surface, which is consistent with the EDS analysis. For the high-resolution Ni 2p, Fe 2p, and W 4 f spectrums in Figs. 2d-2f, we used NiFe-LDH@NFF for comparison to analyze NiFe LDH-CeW@NFF. In Fig. 2d, the two main peaks located at 857.5 and 875.5 eV correspond to Ni $2p_{3/2}$ and Ni $2p_{1/2}$ of Ni(III) whereas the side peaks located near 855.9 and 873.9 eV to Ni $2p_{3/2}$ and Ni $2p_{1/2}$ of Ni(II), respectively [36]. By calculating the ratio of Ni(III)/Ni (II), we can find the NiFe LDH-CeW@NFF shows more Ni(III) than NiFe-LDH@NFF. In Fig. 2e, the two main peaks located near 714.6 and
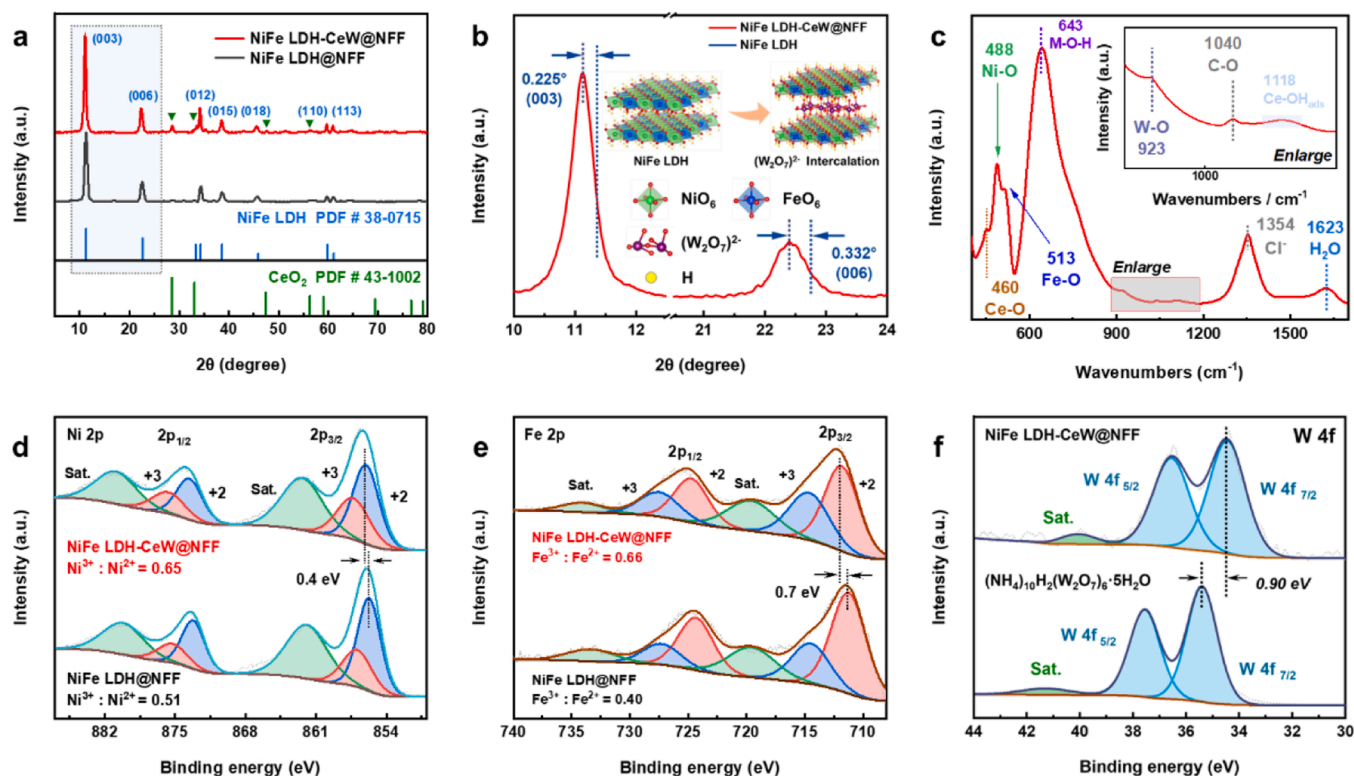

Fig. 2. (a) XRD pattern of NiFe LDH-CeW@NFF and NiFe LDH@NFF with standard patterns of NiFe LDH and CeO_2. (b) Enlargement of partial XRD pattern and the inserted shows the influence by $(W_2O_7)^{2-}$ intercalation. (c) FT-IR spectrum of NiFe LDH-CeW@NFF. XPS spectrums of (d) Ni 2p, (e) Fe 2p, (f) W 4 f.

727.4 eV are attributed to Fe $2p_{3/2}$ and Fe $2p_{1/2}$ of Fe(III) whereas the side peaks located near 711.4 and 724.2 eV to Fe $2p_{3/2}$ and Fe $2p^{1/2}$ of Fe(II), respectively [37]. Similarly, we can find Fe(III) of NiFe LDH-CeW@NFF is more than that of NiFe-LDH@NFF. Besides, compared with the peaks of NiFe-LDH@NFF, the Ni(II) $2p_{3/2}$ and Fe(II) $2p_{3/2}$ peaks of NiFe LDH-CeW@NFF exhibit 0.4 eV and 0.7 eV positive shift in binding energy, respectively. It means the Ni and Fe active sites in NiFe LDH-CeW@NFF show more Lewis acidity. In Fig. 2f, the two main peaks located near 34.6 and 36.6 eV can be ascribed to W $4f_{7/2}$ and W $4f_{5/2}$ of W(VI), respectively [38]. The weak green peaks correspond to the relevant satellite peaks. Compared with the result from $(NH_4)_{10}H_2(W_2O_7)_6 \cdot 5\,H_2O$, the XPS peaks on W 4f for NiFe LDH-CeW@NFF exhibit 0.90 eV negative shift in binding energy, suggesting the decreased valence of W matches well the increased valence of Ni and Fe [39–41]. The Ni and Fe sites with higher valence are conducive to promoting OER [42]. As disclosed by Ce 3d spectrum in Fig. S7, the component of CeO_2 has rich oxygen vacancies (O_{vs}), then we mark it as CeO_2 later [27]. Noted that by comparing XPS spectrums of NiFe LDH-Ce@NFF and NiFe LDH-W@NFF with NiFe LDH-CeW@NFF, it can be found that there is almost no interaction between CeO_2

modification and $(W_2O_7)^{2-}$ intercalation (Fig. S8). The O 1 s in Fig. S9 spectrum can be deconvolved into lattice oxygen (M-O) at 529.7 eV, surface hydroxyl (-OH) at 530.9 eV, O vacancies at 531.7 eV and adsorbed oxygen at 532.8 eV [31]. Compared to NiFe LDH, the oxygen vacancy ratio of NiFe LDH-CeW increases slightly from 22.98% to 29.01%, which might be from the defects in CeO_2. EPR spectra in Fig. S10 indicate that more defects present in NiFe LDH-CeW@NFF and NiFe LDH-Ce@NFF, with the signal located at g = 2.003 typically considered to be oxygen vacancy [31]. Because the signal intensities of NiFe LDH-CeW@NFF and NiFe LDH-Ce@NFF are larger than those of NiFe LDH@NFF and NiFe LDH-W@NFF, revealing the oxygen vacancy in NiFe LDH@NFF is mainly contributed by CeO_2 modification. Studies have confirmed the oxygen vacancies can improve the OER performance [43–45].

2.2. Electrocatalytic OER performance and application in natural seawater

Firstly, the OER activity of catalytic material was assessed in a three-electrode system in 1 M KOH electrolyte. The linear sweep voltammetry
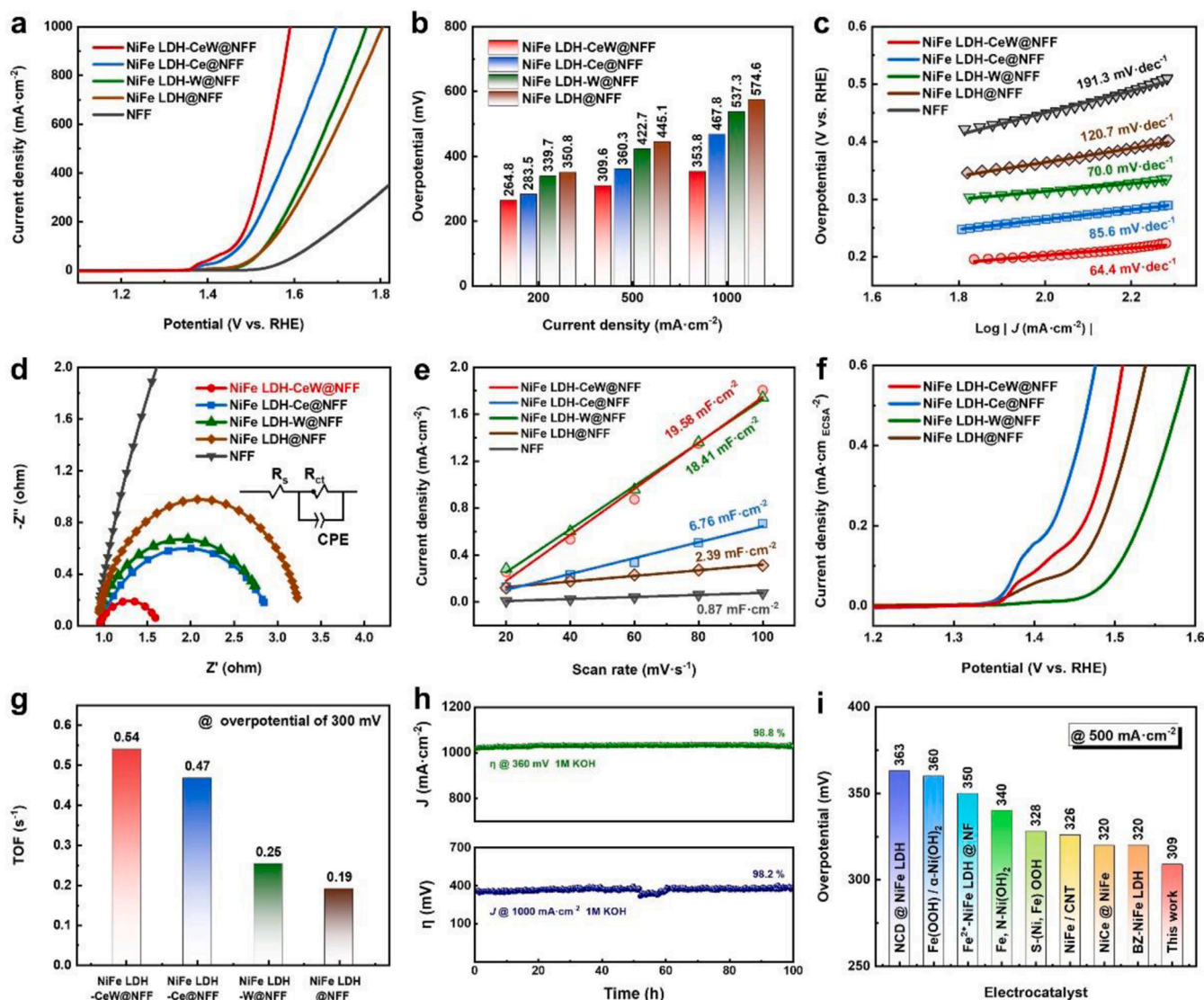

Fig. 3. Compared results of NiFe LDH-CeW@NFF, NiFe LDH-Ce@NFF, NiFe LDH-W@NFF, NiFe LDH@NFF, and NFF: (a) LSV curves, (b) overpotentials at different current densities, (c) Tafel slopes, (d) Nyquist plots, and (e) C_{dl} values for ECSA. (f) ECSA normalized LSV curves and (g) TOF values of the four samples at an overpotential of 300 mV. (h) Chronoamperometric and chronopotentiometric tests on NiFe LDH-CeW@NFF at 1000 mA·cm^{-2} and 0.36 V, respectively. (i) Comparison of overpotentials at high current density of 500 mA·cm^{-2} with other reported OER catalytic materials.

(LSV) curves in Fig. 3a show that the NiFe LDH-CeW@NFF exhibits significantly enhanced OER activity compared with its counterparts of NiFe LDH-Ce@NFF, NiFe LDH-W@NFF, NiFe LDH@NFF and bare NFF. The NiFe LDH-CeW@NFF and NiFe LDH-Ce@NFF catalysts show earlier initial potential values than those of NiFe LDH-W@NFF, NiFe LDH@NFF and bare NFF, which suggests the role of introduced CeO_2 in the composite catalytic material. In addition, the OER activity of NiFe LDH was slightly increased by $(W_2O_7)^{2-}$ intercalation, which may be due to that it expands the layer spacing of LDH and thus increases the electrochemical active specific area. The ultralow overpotentials of 309.6 and 353.8 mV are required to deliver current density of 500 and 1000 mA·cm^{-2}, respectively. Compared with NiFe LDH@NFF, the overpotential decreased by 6.5% after the intercalation of $(W_2O_7)^{2-}$, while the overpotential decreased by 18.6% after the CeO_2 modification. Notably, the overpotential value decreases from 574.6 mV of NiFe LDH@NFF to 353.8 mV of NiFe LDH-CeW@NFF (decreasing by 38%) at 1000 mA·cm^{-2}, showing the synergistic effect of $(W_2O_7)^{2-}$ intercalation and CeO_2 modification (details are shown in Fig. 3b).

Fig. 3c depicts their Tafel plots, in which the NiFe LDH-CeW@NFF has a relatively smaller value of 64.4 mV·dec^{-1} in comparison with those of NiFe LDH-Ce@NFF (85.6 mV·dec^{-1}), NiFe LDH-W@NFF (70.0 mV·dec^{-1}), NiFe LDH@NFF (120.7 mV·dec^{-1}), and bare NFF (191.3 mV·dec^{-1}), reflecting its superior OER catalytic kinetics. We can find NiFe LDH-CeW@NFF and NiFe LDH-W@NFF have lower Tafel slopes, which reveals $(W_2O_7)^{2-}$ intercalation contributes to the improvement of OER dynamics. The exchange current density (j_0) is the current density at the equilibrium potential where the anodic current equals the cathodic current. Fig. S11 shows that NiFe LDH-CeW@NFF has a relatively higher j_0 value of 0.257 mA·cm^{-2} in comparison with those of NiFe LDH-Ce@NFF (0.062 mA·cm^{-2}), NiFe LDH-W@NFF (0.038 mA·cm^{-2}) and NiFe LDH @NFF (0.018 mA·cm^{-2}), suggesting its excellent dynamic characteristics [41]. Furthermore, the electrochemical impedance spectroscopy (EIS) was measured to give insight into the charge transfer kinetics. Fig. 3d shows the charge transfer resistance of the samples with the fitting circuit model inserted. Here, R_{ct} represents the charge-transfer resistance of the catalytic material and R_s represents the internal solution resistance. The NiFe LDH-CeW@NFF has lower R_{ct} of 0.64 Ω than those of NiFe LDH-Ce@NFF (1.82 Ω), NiFe LDH-W@NFF (1.84 Ω), NiFe LDH@NFF (2.30 Ω), and bare NFF (17.26 Ω), which reveals its excellent charge-transfer capability favorable to OER performance. Obviously, CeO_2 can help to reduce the charge transfer resistance, which may be due to the optimization of the electron filling state of e_g level in NiFe-LDH [46]. The electrochemically active surface area (ECSA) of all samples were investigated by using double-layer capacitance (C_{dl}) to estimate the electrocatalytic activity, due to a direct positive correlation between the ECSA and C_{dl} [47]. CV curves at different scanning speeds were measured to calculate the C_{dl} of the catalyst (Fig. S12). In Fig. 3e, NiFe LDH-CeW@NFF (19.6 mF·cm^{-2}) and NiFe LDH-W@NFF (18.4 mF·cm^{-2}) has larger C_{dl} values than other control samples. Fig. 3 f shows the ECSA-normalized LSV curves of the four samples. NiFe LDH-Ce@NFF and NiFe LDH-CeW@NFF show much better activity than other two samples, suggesting the role of CeO_2 modification in improving catalytic activity of NiFe LDH. The TOF value of NiFe LDH-CeW@NFF reaches 0.54 s^{-1} at an overpotential of 300 mV, higher than that of NiFe LDH-Ce@NFF (0.47 s^{-1}), NiFe LDH-W@NFF (0.25 s^{-1}), and NiFe LDH@NFF (0.19 s^{-1}) in Fig. 3 g, revealing its improved instantaneous efficiency for OER [48]. The catalytic stability of NiFe LDH-CeW@NFF was measured by the chronoamperometric and the chronopotentiometric tests in 1 M KOH electrolyte. In Fig. 3 h, the line above nearly remains horizontal with only 1.2% decrease of current density, while the line below tested at 1000 mA·cm^{-2} can still keep for 100 h with 98.2% potential retention compared to its initial value. In addition, it can remain the layer structure after OER process as disclosed by SEM images in Fig. S13. The XPS survey and high-resolution spectrums in Figs. S14 and S15 show similar peaks as the information before cycling. That means, the main components remain. However, the

increased ratios of Ni^{3+} and Fe^{3+} also suggest further oxidation of the material. The above evidences manifest the integrated electrode has robust structure for long-term and large-current-density run although its surface has been oxidized to some degree. Finally, we compared the overpotential values at a large current density of 500 mA·cm^{-2} with recent reported catalytic materials in Fig. 3i, indicating advantage of NiFe LDH-CeW@NFF in large current density, which is the basis of subsequent high current seawater electrolysis (Table S1).

To meet the requirement of practical industrial application, we performed OER tests in simulated alkaline seawater (1 M KOH + 0.5 M NaCl), natural alkaline seawater (1 M KOH + seawater), industrial electrolytic seawater (6 M KOH + seawater), and harsher environment (6 M KOH + seawater with 80 °C) to check the activity and stability of our catalytic material. As shown in Figs. 4a and b, NiFe LDH-CeW@NFF remains the remarkable OER activity in the alkaline simulated seawater, requiring overpotentials of 330.0 and 386.7 mV to deliver current densities of 500 mA·cm^{-2} and 1000 mA·cm^{-2}, respectively. Even we used real seawater instead of 0.5 M NaClin, this electrode with active material shows better activity, requiring overpotentials of 251.4 and 289.8 mV to deliver current densities of 500 mA·cm^{-2} and 1000 mA·cm^{-2}, respectively.

As expected, NiFe LDH-CeW@NFF undoubtedly show much improved activity in 6 M KOH instead of in 1 M KOH especially heating at 80 °C. It only requires overpotentials of 113.5 and 141.6 mV to deliver current densities of 500 mA·cm^{-2} and 1000 mA·cm^{-2}, respectively. Without any iR compensation, the overpotential values are only 271 and 456.6 mV corresponding to the current densities of 500 mA·cm^{-2} and 1000 mA·cm^{-2}, respectively (Fig. S16). Obviously, the overpotentials required to achieve industrial current density of 1000 mA·cm^{-2} are all below 490 mV (threshold for chloride oxidation), suggesting thermodynamically favorable OER process of the NiFe LDH-CeW@NFF anode with undesired CER process at industrially required large current densities. It meets the crucial prerequisite for commercial applications. Notably, under the same KOH concentration, the electrode in natural seawater shows increased overpotential compared with those in simulated seawater or without seawater, which perhaps be due to the distraction from turbid suspension particles, microbes or insoluble precipitates produced during the natural seawater electrolysis process (Fig. 4b). Fig. 4c depicts their Tafel plots, in which NiFe LDH-CeW@NFF has small Tafel slopes of 41.7, 77.9, 66.3, 81.2, 66.0, and 64.9 mV·dec^{-1} in 6 M KOH + seawater (80 °C), 6 M KOH + seawater, 6 M KOH, 1 M KOH + seawater, 1 M KOH + 0.5 M NaCl, and 1 M KOH, respectively. The increased temperature can effectively improve the kinetics. When adding natural seawater instead of 0.5 M NaCl, we can find it hinders the kinetic process of OER. Furthermore, Faraday efficiency is an important index in industrial hydrogen production, which was measured under actual industrial seawater electrolysis (Fig. S17a). When the overpotential is below 490 mV, the Faraday efficiency of NiFe LDH-CeW@NFF is close to 100% (Fig. S17b). Even the overpotential is above 490 mV, the Faraday efficiency is close to 90% (Fig. S17c), suggesting the advantage of NiFe LDH-CeW@NFF for seawater electrooxidation. Examined by the above tests, the activity can meet the requirement for practical seawater electrolysis at high current density, but the stability of the catalytic material even at harsh environment (6 M KOH + 80 °C) needs to be checked. The electrochemical stability of NiFe LDH-CeW@NFF in simulated alkaline seawater (1 M KOH + 0.5 M NaCl) and natural alkaline seawater (1 M KOH + seawater) was measured by chronoamperometric tests. The result in Fig. 4d shows that the performance remains almost stable at a high current density of 1000 mA·cm^{-2} for 100 h with current-density retentions of 99.5% and 98.1% for the system of simulated alkaline seawater and natural alkaline seawater, respectively. Even under harsh conditions, the performance remains almost stable at 1000 mA·cm^{-2} for 48 h in industrial alkaline seawater (6 M KOH + seawater) with retention of 88.6% compared to the initial state. Obviously, the catalytic material was influenced by the harsh environment. But it still gives state-of-the-art stability for
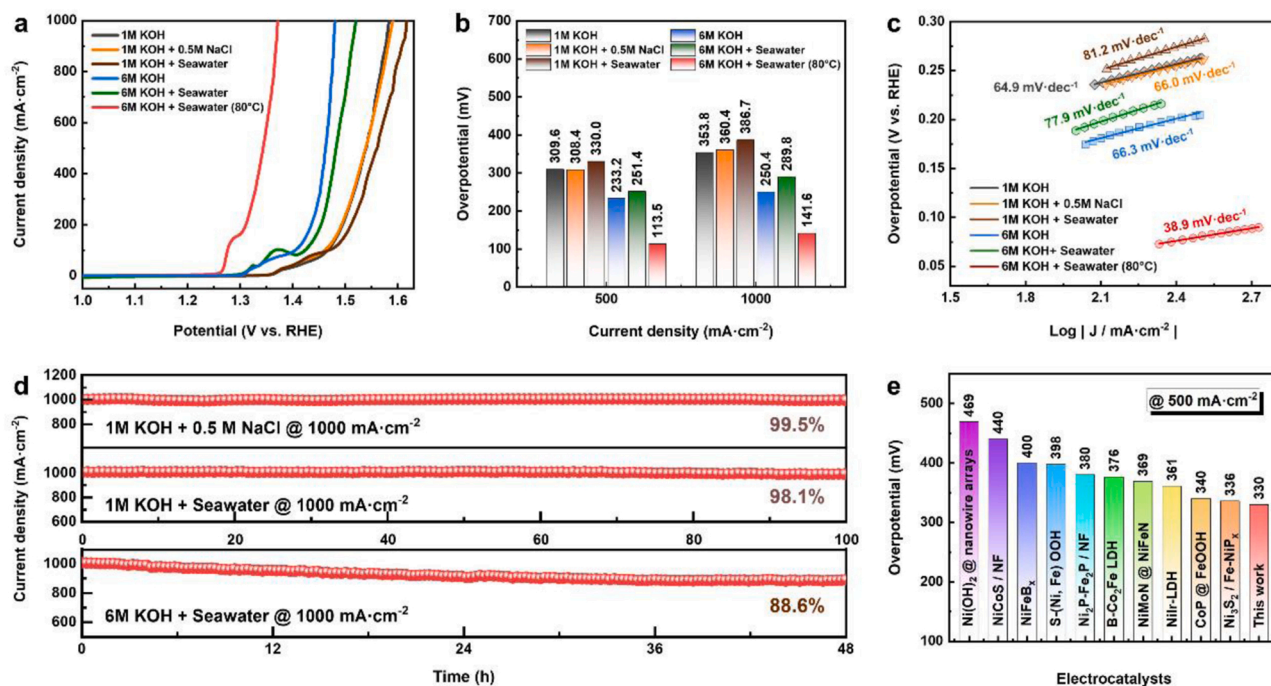
Fig. 4. (a) LSV curves, (b) Comparison of overpotential values, and (c) Tafel slopes of NiFe LDH-CeW@NFF in 1 M KOH, 1 M KOH + 0.5 M NaCl, 1 M KOH + natural seawater, 6 M KOH, 6 M KOH + natural seawater, and 6 M KOH + natural seawater at 80 °C. (d) Chronoamperometric curves of NiFe LDH-CeW@NFF in different media at the current density of 1000 mA·cm⁻². (e) Comparison of overpotential of NiFe LDH-CeW@NFF in 1 M KOH + natural seawater at 500 mA·cm⁻² with recent reported catalytic materials.

industrial seawater electrolysis. Finally, we compared the overpotential values at a large current density of 500 mA·cm⁻² with recent reported catalytic materials in Fig. 4e (Tables S2 and S3).

2.3. Mechanisms on optimized OER performance in seawater

The roles of modified CeO₂ and (W₂O₇)²⁻ anions in improved OER performance were studied. The control experiments above confirmed that the introduced CeO₂ could improve the catalytic performance in
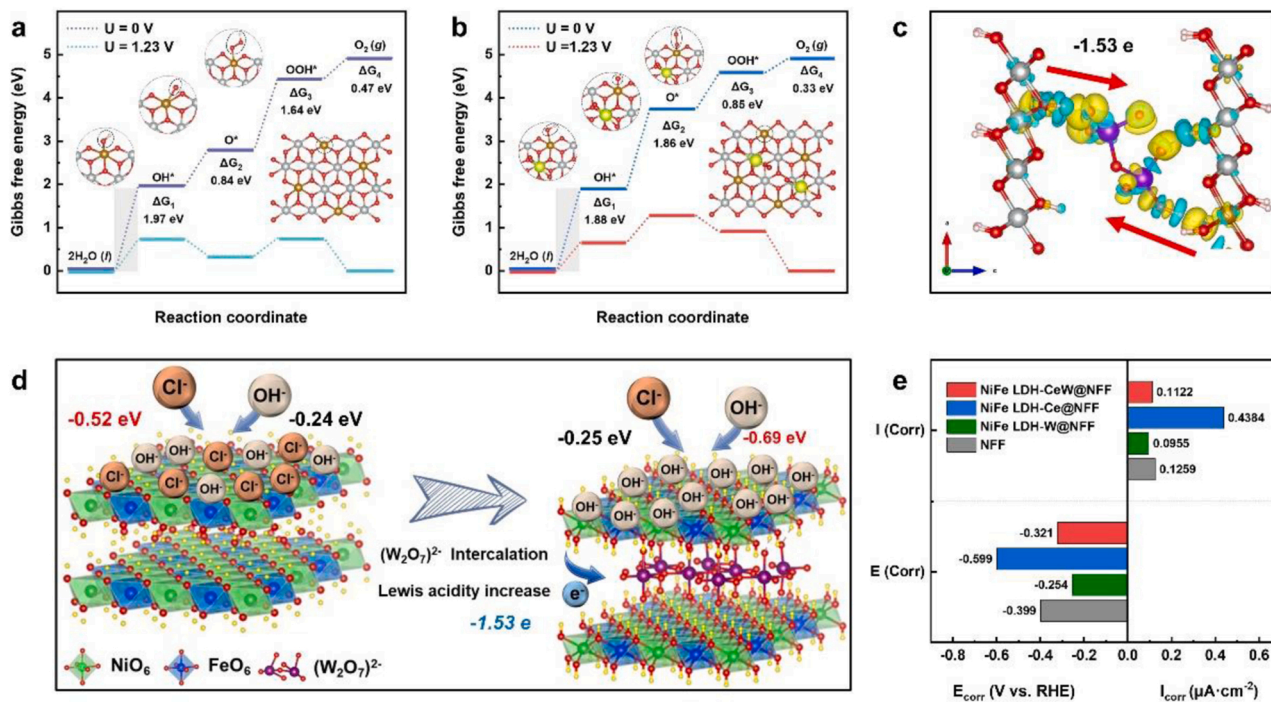

Fig. 5. Gibbs free energy diagram of OER steps on models at U = 1.23 V and U = 0 V of (a) NiFeOOH and (b) NiFeOOH-CeO₂. (c) Differential charge density diagram of (W₂O₇)²⁻-intercalated NiFeOOH. (d) Schematic illustration of HSAB principle and the adsorption energy on OH⁻ and Cl⁻. (e) Corrosion current density and corrosion potential of different samples in natural seawater.

view of the thermodynamics. It has been confirmed by in-situ Raman spectrums in Fig. S18 that NiFe-LDH can easily transform into the component of NiFeOOH, which plays an actual catalytic role in the OER process as many researchers disclose [49]. In addition, the potential that NiFe LDH finishes surface reconstruction decreases from 1.525 to 1.450 V after CeO$_2$ modification and (W$_2$O$_7$)$^{2-}$ intercalation, demonstrating the role of introduced CeO$_2$ and (W$_2$O$_7$)$^{2-}$ in accelerating sample activation during OER process. This accelerated surface reconstruction process can effectively decrease the OER overpotential. Therefore, we used density functional theory (DFT) calculations to confirm the role of CeO$_2$ using two models of NiFeOOH (Fig. 5a) and NiFeOOH-CeO$_2$ (Fig. 5b). According to the ICP results (Table S4), the molar ratio of Ni, Fe, Ce, and W is 60.7%, 23.0%, 9.6%, and 6.7% in NiFe LDH-CeW@NFF. By calculation, the molar ratio of Ni: Fe is close to 3:1. Therefore, we set the value of Ni: Fe to 3:1 in the model of theoretical calculation. The calculated details were presented in Figs. S19-20. We calculated the Gibbs free energies of OH*, O*, and OOH* intermediates along the elementary pathway at U= 0 V and U= 1.23 V. Although both Ni and Fe once were used as catalytic active sites in NiFe LDH system [50–53], we chose Fe here as it is a more stable binding site than Ni during structure optimization. The OH*, O*, and OOH* are preferentially adsorbed on the Fe-sites of NiFeOOH and NiFeOOH-CeO$_2$ during structure optimization. The rate determination step (RDS) might be the first step from H$_2$O to OH* on NiFeOOH with the largest free energy difference of 1.97 eV (Fig. 5a), while the RDS value on Ni, FeOOH-CeO$_2$ has decreased to 1.88 eV (Fig. 5b). Although the adsorption energy on O* increases from 0.84 to 1.86 eV, the other adsorption energies on OOH* and O$_2$ decrease remarkably. Obviously, the introduced CeO$_2$ can reduce energy barriers. In a word, the CeO$_2$ in NiFeOOH can optimally modulate the adsorption free energy barriers on OH*, OOH*, and O$_2$, leading to enhanced OER catalytic activity.

We also studied the advantage of the as-prepared catalytic material with preferential OH$^-$ adsorption (not Cl$^-$ ions) in seawater. We used LSV tests in 1 M KOH + 0.5 M NaCl to test the resistance to Cl$^-$. As disclosed in Fig. S21a, NiFe LDH-CeW@NFF exhibits the smallest overpotential of 308.4 mV at 500 mA cm^{-2}, showing its best anti-chloride ability. Meanwhile, we carried out iodide titration to examine the oxidation product of chlorides (hypochlorite) [54]. The electrolyte turns yellow because I$^-$ was oxidized to I$_2$ by hypochlorite. That is, the solution turns yellower with more hypochlorite. In Fig. S21b, the electrolyte with NiFe LDH-W@NFF and NiFe LDH-CeW@NFF show nearly transparent while other two samples show obvious yellow, revealing (W$_2$O$_7$)$^{2-}$ intercalation can help to improve the selectivity of NiFe LDH towards OH$^-$ in seawater electrolytes. According to the experimental results, (W$_2$O$_7$)$^{2-}$ intercalation can help to enhance the OH$^-$ selectivity in seawater. In theory, W^{6+} as a strong Lewis acid cation can directly promote the increase of the valence states of Ni and Fe (also confirmed by XPS analyses in Fig. 2), and thus increased their Lewis acidity [55]. According to the Pearson's HSAB principle [23], harder acids preferentially bind to harder bases, whereas softer acids bind more strongly to softer bases. Higher valance state means harder Lewis acid for Ni and Fe, while OH$^-$ is a harder base than Cl$^-$ [56]. Therefore, (W$_2$O$_7$)$^{2-}$ intercalation can effectively enhance the selectivity of NiFeOOH to OH$^-$ in seawater electrolyte. DFT calculations also support this theory. Considering the similar layered structure of NiFe-LDH and NiFeOOH, structural models of NiFeOOH (001) crystal planes with and without (W$_2$O$_7$)$^{2-}$ intercalation were established (Figs. S22 and S23). Firstly, it can be observed in the differential charge density diagram (Fig. 5c) that electrons transfer from Ni and Fe sites to W sites (−1.53 e) by adding (W$_2$O$_7$)$^{2-}$, reflecting the increase of the valence states of Ni and Fe, in agreement with the above analysis. Then, the adsorption energies of OH$^-$ and Cl$^-$ on NiFeOOH and (W$_2$O$_7$)$^{2-}$ intercalated NiFeOOH were separately calculated. The results in Fig. 5d show that the adsorption energy of Cl$^-$ and OH$^-$ on the surface of NiFeOOH is − 0.52 and − 0.24 eV respectively, suggesting Cl$^-$ is easier to be adsorbed than OH$^-$, so the pre-catalyst of NiFe-LDH might show poorer OER activity in seawater. When inserting

(W$_2$O$_7$)$^{2-}$, the adsorption energy of Cl$^-$ and OH$^-$ on the surface of (W$_2$O$_7$)$^{2-}$ intercalated NiFeOOH is − 0.25 and − 0.69 eV, suggesting OH$^-$ turns easier to be adsorbed than Cl$^-$, so the pre-catalyst of (W$_2$O$_7$)$^{2-}$ intercalated NiFe-LDH shows superior OER activity in seawater.

In addition, Fig. 5e shows the corrosion current densities and corrosion potentials of the catalytic materials in actual seawater. The data was calculated by extrapolation of the Tafel slopes in Fig. S24. NiFe LDH-W@NFF and NiFe LDH-CeW@NFF have lower corrosion current density and corrected corrosion potential, which directly verifies that the (W$_2$O$_7$)$^{2-}$ intercalation is beneficial to improve the anti-corrosion capability of the catalytic material in natural seawater.

Considering industrial seawater electrolysis operated at high current densities (such as 1000 mA·cm^{-2}), the wetting of the catalytic material in special electrolyte and the rapid release of bubbles from its surface are also important especially at high current densities [57,58]. Therefore, the hydrophilic and repulsive gas properties of the catalytic material were characterized. As shown in Fig. S25, the static contact angle of NiFe LDH-CeW@NFF shows superhydrophilicity (CA = 0°). Compared with that of bare NFF (CA = 126.5°), its hydrophilicity was significantly improved. In addition, the adhesion behavior of oxygen bubbles on the surface of NiFe LDH-CeW@NFF was also tested (Fig. S25, Video S1). Oxygen bubbles can be released from the surface quickly, which confirms the advantage of the material for gas transfer during OER process [59].

Supplementary material related to this article can be found online at doi:10.1016/j.apcatb.2023.122612.

3. Conclusion

In summary, NiFe LDH with CeO$_2$ modification and (W$_2$O$_7$)$^{2-}$ intercalation was synthesized by one-step hydrothermal method. The NiFe LDH-CeW@NFF has excellent catalytic activity, OH$^-$ selectivity and repulsive gas properties, which can catalyze OER efficiently and stably in seawater electrolyte even at large current densities. It needs an overpotential of 353.8 mV in 1 M KOH to require a current density of 1000 mA·cm^{-2} and a Tafel slope as low as 64.4 mV·dec^{-1}. Importantly, it only needs an overpotential of 386.7 mV to give 1000 mA·cm^{-2} in alkaline natural seawater, and can stand more than 100 h with excellent anti-corrosion property. Even operated in harsh industrial scenario (6 M KOH + natural seawater), the catalytic material can remain for 48 h with current density retention up to 88.6%. The reasons for the state-of-the-art activity and stability can be ascribed to the modified CeO$_2$ and inserted (W$_2$O$_7$)$^{2-}$ anions. Control experiments, XPS characterization, and DFT calculations show that the (W$_2$O$_7$)$^{2-}$ intercalation promotes the increase of the valence state of Ni and Fe, which then increases their Lewis acidity. According to HSAB principle, Ni and Fe with higher valence tend to adsorb OH$^-$ instead of Cl$^-$ in seawater electrolyte. Before and after (W$_2$O$_7$)$^{2-}$ intercalation, the adsorption energy on Cl$^-$ changes from − 0.52 to − 0.25 eV, while the value on OH$^-$ turns from − 0.24 to − 0.69 eV. The calculated adsorption energies also confirm our sample with (W$_2$O$_7$)$^{2-}$ intercalation preferentially adsorbs OH$^-$, revealing OH$^-$ selectivity for improved activity and capability of anti-chloride interference. Meanwhile, control experiments and DFT calculations verify that the introduced CeO$_2$ significantly optimizes the adsorption energy on intermediates, reducing the RDS energy of OER process from 1.97 to 1.88 eV. In addition, the catalytic material also shows excellent anti-corrosion and repulsive gas properties in seawater, which provides good stability and fast kinetic process for OER especially at high current densities. The highly efficient and robust OER catalytic material designed in this work show promising application in industrial seawater electrolysis.

CRediT authorship contribution statement

Mingzhe Li: Conceptualization, Experiments, Writing – original draft, Methodology, Investigation. **Hua-Jie Niu:** Paper logic, Writing –

review and editing. **Yilong Li:** Experiments. **Jiawei Liu:** Investigation. **Xiayuan Yang:** Investigation. **Yuzhen Lv:** Funding acquisition, Project administration, Conceptualization, Resources, Supervision. **Kepi Chen:** Resources. **Wei Zhou:** Experimental discussion, Writing – review and editing.

Declaration of Competing Interest

The authors declare that they have no known competing financial interests or personal relationships that could have appeared to influence the work reported in this paper.

Data availability

Data will be made available on request.

Acknowledgements

Appendix A. Supporting information

Supplementary data associated with this article can be found in the online version at doi:10.1016/j.apcatb.2023.122612.

References

[1] M.A. Khan, H. Zhao, W. Zou, Z. Chen, W. Cao, J. Fang, J. Xu, L. Zhang, J. Zhang, Recent progresses in electrocatalysts for water electrolysis, Electrochem. Energy Rev. 1 (2018) 483–530.

[2] S. Dresp, F. Dionigi, M. Klingenhof, P. Strasser, Direct electrolytic splitting of seawater: opportunities and challenges, ACS Energy Lett. 4 (2019) 933–942.

[3] D.V. Esposito, Membraneless electrolyzers for low-cost hydrogen production in a renewable energy future, Joule 1 (2017) 651–658.

[4] Y. Luo, Z. Zhang, M. Chhowalla, B. Liu, Recent advances in design of electrocatalysts for high-current-density water splitting, Adv. Mater. 34 (2022), e2108133.

[5] D. Guan, W. Zhou, Z. Shao, Rational design of superior electrocatalysts for water oxidation: crystalline or amorphous structure? Small Sci. 1 (2021) 2100030.

[6] L. Tan, J. Yu, C. Wang, H. Wang, X. Liu, H. Gao, L. Xin, D. Liu, W. Hou, T. Zhan, Partial sulfidation strategy to NiFe-LDH@FeNi$_2$S$_4$ heterostructure enable high-performance water/seawater oxidation, Adv. Funct. Mater. 32 (2022) 2200951.

[7] F. Dionigi, T. Reier, Z. Pawolek, M. Gliech, P. Strasser, Design criteria, operating conditions, and nickel-iron hydroxide catalyst materials for selective seawater electrolysis, ChemSusChem 9 (2016) 962–972.

[8] J.S. Kim, B. Kim, H. Kim, K. Kang, Recent progress on multimetal oxide catalysts for the oxygen evolution reaction, Adv. Energy Mater. 8 (2018) 1702774.

[9] F. Zhang, L. Yu, L. Wu, D. Luo, Z. Ren, Rational design of oxygen evolution reaction catalysts for seawater electrolysis, Trends Chem. 3 (2021) 485–498.

[10] L. Yu, L. Wu, B. McElhenny, S. Song, D. Luo, F. Zhang, Y. Yu, S. Chen, Z. Ren, Ultrafast room-temperature synthesis of porous S-doped Ni/Fe (oxy)hydroxide electrodes for oxygen evolution catalysis in seawater splitting, Energy Environ. Sci. 13 (2020) 3439–3446.

[11] R. Gao, D. Yan, Recent development of Ni/Fe-based micro/nanostructures toward photo/electrochemical water oxidation, Adv. Energy Mater. 10 (2019) 1900954.

[12] S. Dresp, F. Dionigi, M. Klingenhof, T. Merzdorf, H. Schmies, J. Drnec, A. Poulain, P. Strasser, Molecular understanding of the impact of saline contaminants and alkaline pH on NiFe layered double hydroxide oxygen evolution catalysts, ACS Catal. 11 (2021) 6800–6809.

[13] Y. Wang, D. Yan, S. El Hankari, Y. Zou, S. Wang, Recent progress on layered double hydroxides and their derivatives for electrocatalytic water splitting, Adv. Sci. 5 (2018) 1800064.

[14] L. Lv, Z. Yang, K. Chen, C. Wang, Y. Xiong, 2D layered double hydroxides for oxygen evolution reaction: from fundamental design to application, Adv. Energy Mater. 9 (2019) 1803358.

[15] Z.W. Seh, J. Kibsgaard, C.F. Dickens, I. Chorkendorff, J.K. Norskov, T.F. Jaramillo, Combining theory and experiment in electrocatalysis: insights into materials design, Science 355 (2017) eaad4998.

[16] Y. Kuang, M.J. Kenney, Y. Meng, W.H. Hung, Y. Liu, J.E. Huang, R. Prasanna, P. Li, Y. Li, L. Wang, M.C. Lin, M.D. McGehee, X. Sun, H. Dai, Solar-driven, highly sustained splitting of seawater into hydrogen and oxygen fuels, Proc. Natl. Acad. Sci. U. S. A. 116 (2019) 6624–6629.

[17] L. Yu, Q. Zhu, S. Song, B. McElhenny, D. Wang, C. Wu, Z. Qin, J. Bao, Y. Yu, S. Chen, Z. Ren, Non-noble metal-nitride based electrocatalysts for high-performance alkaline seawater electrolysis, Nat. Commun. 10 (2019) 5106.

[18] Q. Tu, W. Liu, M. Jiang, W. Wang, Q. Kang, P. Wang, W. Zhou, F. Zhou, Preferential adsorption of hydroxide ions onto partially crystalline NiFe-layered double hydroxides leads to efficient and selective OER in alkaline seawater, ACS Appl. Energy Mater. 4 (2021) 4630–4637.

[19] H. Xu, B. Wang, C. Shan, P. Xi, W. Liu, Y. Tang, Ce-doped NiFe-layered double hydroxide ultrathin nanosheets/nanocarbon hierarchical nanocomposite as an efficient oxygen evolution catalyst, ACS Appl. Mater. Interfaces 10 (2018) 6336–6345.

[20] J.X. Feng, S.H. Ye, H. Xu, Y.X. Tong, G.R. Li, Design and synthesis of FeOOH/CeO$_2$ heterolayered nanotube electrocatalysts for the oxygen evolution reaction, Adv. Mater. 31 (2019), e1904188.

[21] J. Ding, Y. Han, G. Hong, Tailoring the activity of NiFe layered double hydroxide with CeCO$_3$OH as highly efficient water oxidation electrocatalyst, Int. J. Hydrog. Energy 46 (2021) 2018–2025.

[22] H. Sun, J. Sun, Y. Song, Y. Zhang, Y. Qiu, M. Sun, X. Tian, C. Li, Z. Lv, L. Zhang, Nickel-cobalt hydrogen phosphate on nickel nitride supported on nickel foam for alkaline seawater electrolysis, ACS Appl. Mater. Interfaces 14 (2022) 22061–22070.

[23] B.G. Pearson, Hard and soft acids and bases, J. Am. Chem. Soc. 85 (1963) 3533–3539.

[24] P.-F. Guo, Y. Yang, W.-J. Wang, B. Zhu, W.-T. Wang, Z.-Y. Wang, J.-L. Wang, K. Wang, Z.-H. He, Z.-T. Liu, Stable and active NiFeW layered double hydroxide for enhanced electrocatalytic oxygen evolution reaction, Chem. Eng. J. 426 (2021), 130768.

[25] R. Rajendiran, D. Chinnadurai, K. Chen, A.R. Selvaraj, K. Prabakar, O.L. Li, Electrodeposited trimetallic NiFeW hydroxide electrocatalysts for efficient water oxidation, ChemSusChem 14 (2021) 1324–1335.

[26] E.L. Lawrence, S.L.Y. Chang, P.A. Crozier, In situ tem observations of oxygen surface dynamics in CeO$_2$ cubes, Microsc. Microanal. 23 (2017) 1994–1995.

[27] M. Liu, K.A. Min, B. Han, L.Y.S. Lee, Interfacing or doping? Role of Ce in highly promoted water oxidation of NiFe-layered double hydroxide, Adv. Energy Mater. 11 (2021) 2101281.

[28] M.A. Pugachevskii, A.N. Chibisov, V.A. Mamontov, A.P. Kuzmenko, Antioxidant properties of stabilized CeO$_2$ nanoparticles, Phys. Status Solidi A 218 (2021) 2100355.

[29] Z. Liu, N. Li, H. Zhao, Y. Zhang, Y. Huang, Z. Yin, Y. Du, Regulating the active species of Ni(OH)$_2$ using CeO$_2$: 3D CeO$_2$/Ni(OH)$_2$/carbon foam as an efficient electrode for the oxygen evolution reaction, Chem. Sci. 8 (2017) 3211–3217.

[30] D. Wang, F.-X. Yin, B. Cheng, Y. Xia, J.-G. Yu, W.-K. Ho, Enhanced photocatalytic activity and mechanism of CeO$_2$ hollow spheres for tetracycline degradation, Rare Met. 40 (2021) 2369–2380.

[31] M. Ying, X. Lin, G. Yang, H. Ye, H. Pan, M. Du, Rich oxygen vacancies on ultrathin NiFe layered double hydroxide nanosheets raised by cerium-assisted synthesis for enhanced electrocatalytic water oxidation, Colloids Surf. A Physicochem. Eng. Asp. 627 (2021), 127142.

[32] S. Aisawa, H. Hirahara, H. Uchiyama, S. Takahashi, E. Narita, Synthesis and thermal decomposition of Mn-Al layered double hydroxides, J. Solid State Chem. 167 (2002) 152–159.

[33] R. Rao, Y. Huang, Q. Ling, C. Hu, X. Dong, J. Xiang, Q. Zhou, S. Fang, Y. Hu, Y. Zhang, Q. Tang, A facile pyrolysis synthesis of Ni doped Ce$_2$O$_3$@CeO$_2$/CN composites for adsorption removal of congo red: Activation of carbon nitride structure, Sep. Purif. Technol. 305 (2023), 122505.

[34] S. Sanati, Z. Rezvani, Ultrasound-assisted synthesis of NiFe-layered double hydroxides as efficient electrode materials in supercapacitors, Ultrason. Sonochem. 48 (2018) 199–206.

[35] W. Thitsartarn, S. Kawi, An active and stable CaO-CeO$_2$ catalyst for transesterification of oil to biodiesel, Green. Chem. 13 (2011) 3423–3430.

[36] Y. Yan, R. Zhang, Y. Yu, Z. Sun, R. Che, B. Wei, A.P. LaGrow, Z. Wang, W. Zhou, Interfacial optimization of PtNi octahedrons@Ti$_3$C$_2$ mxene with enhanced alkaline hydrogen evolution activity and stability, Appl. Catal. B 291 (2021), 120100.

[37] Y. Tang, Q. Liu, L. Dong, H.B. Wu, X.-Y. Yu, Activating the hydrogen evolution and overall water splitting performance of NiFe LDH by cation doping and plasma reduction, Appl. Catal. B 266 (2020), 118627.

[38] R. Juškėnas, I. Valsiūnas, V. Pakštas, A. Selskis, V. Jasulaitienė, V. Karpavičienė, V. Kapočius, XRD, XPS and AFM studies of the unknown phase formed on the surface during electrodeposition of Ni-W alloy, Appl. Surf. Sci. 253 (2006) 1435–1442.

[39] L. Trotochaud, S.L. Young, J.K. Ranney, S.W. Boettcher, Nickel-iron oxyhydroxide oxygen-evolution electrocatalysts: the role of intentional and incidental iron incorporation, J. Am. Chem. Soc. 136 (2014) 6744–6753.

[40] J.B. Gerken, S.E. Shaner, R.C. Massé, N.J. Porubsky, S.S. Stahl, A survey of diverse earth abundant oxygen evolution electrocatalysts showing enhanced activity from Ni-Fe oxides containing a third metal, Energy Environ. Sci. 7 (2014) 2376–2382.

[41] H.-J. Niu, Y. Yan, S. Jiang, T. Liu, T. Sun, W. Zhou, L. Guo, J. Li, Interfaces decrease the alkaline hydrogen-evolution kinetics energy barrier on NiCoP/Ti$_3$C$_2$T$_x$ MXene, ACS Nano 16 (2022) 11049–11058.

[42] M. Han, N. Wang, B. Zhang, Y. Xia, J. Li, J. Han, K. Yao, C. Gao, C. He, Y. Liu, Z. Wang, A. Seifitokaldani, X. Sun, H. Liang, High-valent nickel promoted by atomically embedded copper for efficient water oxidation, ACS Catal. 10 (2020) 9725–9734.

[43] R. Liu, Y. Wang, D. Liu, Y. Zou, S. Wang, Water-plasma-enabled exfoliation of ultrathin layered double hydroxide nanosheets with multivacancies for water oxidation, Adv. Mater. 29 (2017) 1701546.

[44] Z. Cai, Z. Bi, E. Hu, W. Liu, N. Dwarica, Y. Tian, X. Li, Y. Kuang, Y. Li, X.Q. Yang, H. Wang, X. Sun, Single-crystalline ultrathin Co$_3$O$_4$ nanosheets with massive

vacancy defects for enhanced electrocatalysis, Adv. Energy Mater. 8 (2017) 1701694.

[45] T. Liu, A. Li, W. Zhou, C. Lyu, Hierarchical nano/micro/macro-assembled integrated electrode with high-performance water electro-oxidation, Chem. Eng. J. 415 (2021), 128941.

[46] Y. Guo, Y. Tong, P. Chen, K. Xu, J. Zhao, Y. Lin, W. Chu, Z. Peng, C. Wu, Y. Xie, Engineering the electronic state of a perovskite electrocatalyst for synergistically enhanced oxygen evolution reaction, Adv. Mater. 27 (2015) 5989–5994.

[47] C. Wang, L. Chai, Q. Tian, S. Liu, A simple preparation of Co0.75Fe0.25 hydrous oxide nanoparticles as active electrocatalysts for water oxidation reaction, Int. J. Energy Res. 44 (2020) 7820–7830.

[48] S. Liu, S. Ren, R.-T. Gao, X. Liu, L. Wang, Atomically embedded Ag on transition metal hydroxides triggers the lattice oxygen towards sustained seawater electrolysis, Nano Energy 98 (2022), 107212.

[49] J. Kang, Y. Xue, J. Yang, Q. Hu, Q. Zhang, L. Gu, A. Selloni, L.M. Liu, L. Guo, Realizing two-electron transfer in Ni(OH)$_2$ nanosheets for energy storage, J. Am. Chem. Soc. 144 (2022) 8969–8976.

[50] D. Friebel, M.W. Louie, M. Bajdich, K.E. Sanwald, Y. Cai, A.M. Wise, M.J. Cheng, D. Sokaras, T.C. Weng, R. Alonso-Mori, R.C. Davis, J.R. Bargar, J.K. Norskov, A. Nilsson, A.T. Bell, Identification of highly active Fe sites in (Ni,Fe)OOH for electrocatalytic water splitting, J. Am. Chem. Soc. 137 (2015) 1305–1313.

[51] N. Li, D.K. Bediako, R.G. Hadt, D. Hayes, T.J. Kempa, F. von Cube, D.C. Bell, L. X. Chen, D.G. Nocera, Influence of iron doping on tetravalent nickel content in catalytic oxygen evolving films, Proc. Natl. Acad. Sci. U. S. A. 114 (2017) 1486–1491.

[52] J.Y. Chen, L. Dang, H. Liang, W. Bi, J.B. Gerken, S. Jin, E.E. Alp, S.S. Stahl, Operando analysis of NiFe and fe oxyhydroxide electrocatalysts for water oxidation: Detection of Fe4+ by mossbauer spectroscopy, J. Am. Chem. Soc. 137 (2015) 15090–15093.

[53] B.M. Hunter, N.B. Thompson, A.M. Müller, G.R. Rossman, M.G. Hill, J.R. Winkler, H.B. Gray, Trapping an iron(VI) water-splitting intermediate in nonaqueous media, Joule 2 (2018) 747–763.

[54] Z. Wang, C. Wang, L. Ye, X. Liu, L. Xin, Y. Yang, L. Wang, W. Hou, Y. Wen, T. Zhan, MnO$_x$ film-coated NiFe-LDH nanosheets on Ni foam as selective oxygen evolution electrocatalysts for alkaline seawater oxidation, Inorg. Chem. 61 (2022) 15256–15265.

[55] P.D. Frémont, N. Adet, J. Parmentier, X.J. Xu, B. Jacques, S. Dagorne, Cationic organometallic complexes of group 12 metals: a decade of progress toward the quest of novel Lewis acidic catalysts, Coordin, Chem. Rev. 469 (2022), 214647.

[56] B.M. Hunter, W. Hieringer, J.R. Winkler, H.B. Gray, A.M. Müller, Effect of interlayer anions on [NiFe]-LDH nanosheet water oxidation activity, Energy Environ. Sci. 9 (2016) 1734–1743.

[57] Y. Luo, L. Tang, U. Khan, Q. Yu, H.M. Cheng, X. Zou, B. Liu, Morphology and surface chemistry engineering toward pH-universal catalysts for hydrogen evolution at high current density, Nat. Commun. 10 (2019) 269.

[58] X. Shen, H. Li, Y. Zhang, T. Ma, Q. Li, Q. Jiao, Y. Zhao, H. Li, C. Feng, Construction dual-regulated NiCo$_2$S$_4$@Mo-doped CoFe-LDH for oxygen evolution reaction at large current density, Appl. Catal. B 319 (2022), 121917.

[59] M. Wang, Y. Wu, N. Li, F. Zhao, Q. Zhao, J. Li, G. Liu, Synergistic assembly of a CoS@NiFe/Ni foam heterostructure electrocatalyst for efficient water oxidation catalysis at large current densities, Chem. Asian J. 15 (2020) 1484–1492.